Dynamics in the center manifold around equilibrium points periodically perturbed three-body problems

Bastien Le Bihan, Josep Masdemont, Gérard Gómez, Stéphanie Lizy-Destrez

DYNAMICS IN THE CENTER MANIFOLD AROUND EQUILIBRIUM POINTS IN PERIODICALLY PERTURBED THREE-BODY PROBLEMS

Bastien Le Bihan[1], *Josep Masdemont*[2], *Gerard Gómez*[3], *Stéphanie Lizy-Destrez*[1]

[1] ISAE-SUPAERO, 10 av. Edouard Belin - BP 54032 - 31055 Toulouse Cedex 4, France

[2] IEEC & Departament de Matemàtica Aplicada I, ETSEIB, Universitat Politècnica de Catalunya, Diagonal 647, 08028 Barcelona, Spain

[3] IEEC & Departament de Matemàtica Aplicada i Anàlisi, Universitat de Barcelona, Gran Via 585, 08007 Barcelona, Spain

ABSTRACT

A new application of the parameterization method is presented to compute invariant manifolds about the equilibrium points of Periodically Perturbed Three-Body Problems (PPTBP). These techniques are applied to obtain high-order semi-numerical approximations of the center manifolds about the points $L_{1,2}$ of the Sun-perturbed Earth-Moon Quasi-Bicicular Problem (QBCP), which is a particular case of PPTBP. The quality of these approximations is compared with results obtained using equivalents of previous normal form procedures. Then, the parameterization is used to initialize the computation of Poincaré maps, which allow to get a qualitative description of the periodically-perturbed dynamics near the equilibrium points.

***Index Terms*—** parameterization method, center manifold, four-body model, quasi-bicircular problem, Sun-Earth-Moon system

1. INTRODUCTION

The present paper is part of a project which aims to provide a systematic or near-systematic analysis tool for the motion of a spacecraft about and between the libration points of the Sun-perturbed Earth-Moon system. The dynamics around the Earth-Moon (EM) and Sun-(Earth+Moon) (SEM) collinear libration points L_1 and L_2 are of notable interest. In that context, the literature mainly addresses two four-body models:

A. The Bicircular problem (BCP)**.** Widely used for the study of the EM triangular libration points [1,2] and for transfer optimization [3–5], it considers the Earth and the Moon moving in circular orbits around their barycenter which is moving in circular orbit around the Sun. Such a model is not coherent since the motion of the three primaries is not a solution of the corresponding three-body problem.

B. The Quasi-Bicircular problem (QBCP)**.** This is a bicircular coherent periodic model that has been developed in [6]. In this framework, the motion of the three primaries is a planar self-consistent solution of the three-body problem along quasi-circular orbits.

Both the BCP and the QBCP provide an all-in-one solution for the study of the dynamics in the Sun-Earth-Moon system. In the present paper, emphasis is made on the collinear libration points L_1 and L_2, in particular in the Earth-Moon system. Consequently, the QBCP is selected given (i) its coherent nature and (ii) the slightly broader literature available on the subject. Comparisons with results in the BCP are envisaged in the near future.

The description of the phase space around these collinear libration points has been done in the past, either in the Sun-Earth or the Earth-Moon case, and both through pure numerical techniques [7] and semi-analytical procedures [2,6,8,11,12].

As the reader may know, the span of the semi-numerical approaches are naturally limited since the resulting expansions are not convergent in any open set. However, there usually exists a domain of practical convergence within which the series are seemingly convergent for numerical purposes. In such a domain, they can provide a very compact tool to describe the phase space.

In this paper, the parameterization method is extended to the QBCP framework in order to compute the center manifold of the libration points $L_{1,2}$ of the Earth-Moon system.

In section 2, the QBCP is introduced along with the corresponding equations of motion. Then, the extension of the parameterization method to the time-periodic domain requires a suitable form for the linearized vector field, as detailed in section 3.

Section 4 details the building blocks of the parameterization method, with the example of the center manifold of $\text{EML}_{1,2}$ as a guideline. It is shown that the normal form procedure can still be seen as a subclass (or *style*) of parameterization methods as in the autonomous case [12].

In section 5, the case of the center manifold of $\text{EML}_{1,2}$ is detailed along with numerical results. Two different styles of

parameterization are quantitatively compared : the graph and normal form styles. In the EML_2 case, the graph style proves to be useful to partially handle resonances that act as natural obstructions to the semi-analytical normal form. Finally, the approximations of the center manifolds are used to initialize the computation of Poincaré maps. The graph style proves again to be convenient to quickly integrate the equations of motion in the center manifold.

Note that a more complete description of the procedure at hand will be made available in a work under progress [13].

2. THE QUASI-BICIRCULAR PROBLEM

The Quasi-Bicircular Problem (QBCP) is a restricted four-body problem introduced by [6] to describe the motion of a massless spacecraft subjected to the gravitational influence of the Earth, Moon, and Sun, whose own motion is a quasi-bicircular solution of the Three-Body Problem. The resulting system is an Hamiltonian with three degrees of freedom and depending periodically on time. This Hamiltonian takes a simple form when derived in specific synodical systems of reference. As an example, the EM synodical frame is a rotating-pulsating frame centered at the Earth-Moon barycenter B_{em} in such a way that the Earth and the Moon are located at fixed points, as in the usual CRTBP synodical frame (see Figure 1).

Denoting the state by $\mathbf{z} = (x\ y\ z\ p_x\ p_y\ p_z)^T$ in such a frame, the Hamiltonian of the QBCP takes the form:

$$\begin{aligned} H(\mathbf{z},\theta) = &\frac{1}{2}\alpha_1(p_x^2+p_y^2+p_z^2) + \alpha_2(p_x x + p_y y + p_z z) \\ &+ \alpha_3(p_x y - p_y x) + \alpha_4 x + \alpha_5 y \\ &- \alpha_6\left(\frac{1-\mu}{q_{pe}} + \frac{\mu}{q_{pm}} + \frac{m_s}{q_{ps}}\right) \end{aligned} \tag{1}$$

where:

$$\begin{aligned} q_{pe}^2 &= (x-\mu)^2 + y^2 + z^2 \\ q_{pm}^2 &= (x-\mu+1)^2 + y^2 + z^2 \\ q_{ps}^2 &= (x-\alpha_7)^2 + (y-\alpha_8)^2 + z^2 \end{aligned}$$

with μ the Earth-Moon mass ratio, and m_s the mass of the Sun. Moreover, the α_k are trigonometric functions in the variable $\theta = \omega_s t$ where ω_s is the pulsation of the Sun. The first coefficients of these functions are available in [6]. This Hamiltonian is T-periodic with respect to the time t, with $T = 2\pi/\omega_s$.

In the QBCP, due to the effect of the Sun, the libration points are no longer equilibrium points. They are replaced by periodic orbits with the same frequency as the perturbation (see [9] for the theoretical justification in the $L_{4,5}$ BCP case). The so-called dynamical equivalents of $\text{EML}_{1,2}$ are given on Figure 2, along with the position of their CRTBP counterparts.

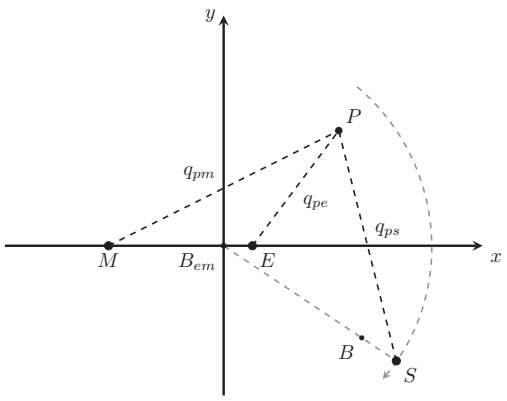

Fig. 1: The QBCP in the synodical EM synodical reference frame. B is the barycenter of the system (adapted from [14]).

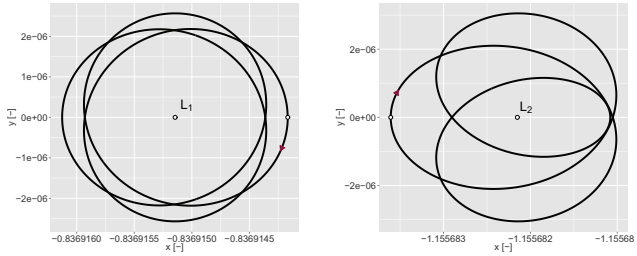

(a) L_1 case (b) L_2 case

Fig. 2: T-periodic orbits that act as dynamical equivalents of the Earth-Moon libration points $L_{1,2}$, in EM coordinates. The central $\circ$ symbol is the CRTBP geometric position of the libration point. The starting point at $t = 0$ is plotted on each orbit as well as the direction of motion for $t > 0$ (red arrow).

3. A SUITABLE FORM FOR THE LINEARIZED VECTOR FIELD

The so-called *parameterization method* (PM) has been previously used to compute high-order power series expansions of parameterizations of invariant manifolds of vector fields at fixed points [15]. An iconic example is the computation of the center manifold of the Earth-Moon libration point L_1 in the CRTBP [12]. This paper extends such approach to invariant manifolds of periodically-perturbed vector fields about a periodic orbit with the same frequency.

The first step of such extension is to put the linearized vector field into a form equivalent to the autonomous case. Namely, this requires the origin to be a fixed point and the linearized vector field to be both diagonal and autonomous at this origin. These features can be obtained by applying a suitable change of coordinates, as explained below.

3.1. Corresponding change of coordinates

For a system described by a periodically-perturbed Hamiltonian, a change of coordinates that leaves the linearized vector field in proper form can be obtained by implementing the following steps:

1. Autonomize the Hamiltonian by introducing the canonical couple of variables (θ, y_θ) so that the time is managed as a new variable. This is done by simply adding the term $\omega_s y_\theta$ to the initial Hamiltonian, forming an extended autonomous Hamiltonian system of degree four.
2. Cancel the terms of order one or, equivalently, translate the origin of coordinates to the periodic orbit which substitutes $L_{1,2}$ so that the origin becomes a fixed point.
3. Compute a normal form for the terms of order two, using Floquet theorem. In particular, the differential of the vector field evaluated at the origin will be time-independent.
4. Use a complexification of the state to get a true diagonal form for the order two.

Such procedure is thoroughly described in [6] in the QBCP Earth-Moon L_2 case, and in [2] in the BCP $L_{3,4,5}$ case. In brief, the composition of these operations defines a change of coordinates, denoted COC, of the form:

$$\begin{cases} \mathbf{z} = P_c(\theta)\hat{\mathbf{z}} + V(\theta) \\ \theta = \hat{\theta} \\ y_\theta = \hat{y}_\theta + p_0(\theta) + p_1(\hat{\mathbf{z}}, \theta) + p_2(\hat{\mathbf{z}}, \theta) \end{cases} \tag{2}$$

where p_0 is a 2π-periodic function, $p_{1,2}$ are linear functions in $\hat{\mathbf{z}}$, p is a complex 6×6 matrix, and V is a real 6×1, all with 2π-periodic coefficients. The final coordinates $\hat{\mathbf{z}} = \left(\hat{\mathbf{x}}^T\ \hat{\mathbf{y}}^T\right)^T = \left(\hat{x}_1\ \hat{x}_2\ \hat{x}_3\ \hat{y}_1\ \hat{y}_2\ \hat{y}_3\right)^T$ are denoted Translated-Floquet-Complexified (TFC). In these coordinates, the Hamiltonian $\hat{H}$ takes the form:

$$\begin{aligned} \hat{H}(\hat{\mathbf{z}}, \hat{\theta}, \hat{y}_\theta) = \omega_s \hat{y}_\theta + \omega_1 \mathbf{i} \hat{x}_1 \hat{y}_1 + \omega_2 \hat{x}_2 \hat{y}_2 + \omega_3 \mathbf{i} \hat{x}_3 \hat{y}_3 \\ + \sum_{k \geq 3} \hat{H}_k(\hat{\mathbf{z}}, \hat{\theta}) \end{aligned} \tag{3}$$

where $\omega_i, i \in [\![1, 3]\!]$ are real coefficients given in Table 1 for the $\text{EML}_{1,2}$ case. Moreover, the terms $H_k(\hat{\mathbf{z}}, \hat{\theta})$ for $k \geq 3$ are homogeneous Fourier-Taylor polynomials of degree k in the complex variable $\hat{\mathbf{z}}$ that are not explicitly available at this step.

In practice, only the first line of equation (2) is incorporated into the numerical implementation.

3.2. Corresponding vector field

The change of variables (2) provides an Hamiltonian $\hat{H}$ in autonomous diagonal form at order 2. From this form, the corresponding vector field can be derived and plugged into the parameterization method:

Table 1: The coefficients ω_i that appear in equation (3), in the Earth-Moon $L_{1,2}$ case. All values are given with the same precision as in [6].

ω_i	L_1	L_2
ω_1	$-4.38968496\text{e}{-01}$	$+1.34709423\text{e}{-02}$
ω_2	$+2.93720564\text{e}{+00}$	$+2.16306748\text{e}{+00}$
ω_3	$+4.22768254\text{e}{-01}$	$-6.02217885\text{e}{-02}$

$$\dot{\hat{\mathbf{z}}} = \hat{F}(\hat{\mathbf{z}}, \theta) = \begin{pmatrix} \Omega & 0 \\ 0 & -\Omega \end{pmatrix} \begin{pmatrix} \hat{\mathbf{x}} \\ \hat{\mathbf{y}} \end{pmatrix} + \sum_{k=3}^{\infty} J \nabla \hat{H}_k(\hat{\mathbf{z}}, \theta) \tag{4}$$

with

$$\Omega = \begin{pmatrix} \mathbf{i}\omega_1 & 0 & 0 \\ 0 & \omega_2 & 0 \\ 0 & 0 & \mathbf{i}\omega_3 \end{pmatrix}, \quad J = \begin{pmatrix} 0 & I_3 \\ -I_3 & 0 \end{pmatrix}$$

The linearized part of (4) has the desired autonomous diagonal form for the initialization of the parameterization method. Moreover, the TFC origin is naturally a fixed point and all the conditions defined at the beginning of this section are satisfied.

3.3. Precision of the COC

At this point, one can see that the overall accuracy of the change of coordinates (2) directly depends on the precision with which the periodic coefficients in P_c and V are computed. In practice, these coefficients are obtained by a Fourier analysis of 2π-periodic functions integrated along the dynamical equivalent of the libration point (see [2, 13]). As in the three-body case, the linear dynamics about the collinear points is a cross product of two centers, and one saddle $\times$ associated with a pair of real positive eigenvalues. Naturally, the precision of the integration of the periodic coefficients is limited by the magnitude of the hyperbolic unstable direction associated to the orbit.

To estimate this constraint, let λ_u be the eigenvalue associated with the unstable direction. Then an initial error $\epsilon(0)$ made along the unstable direction leads, after a time t, to an error:

$$\epsilon(t) \sim \epsilon(0) e^{\frac{t}{T} \ln(\lambda_u)} = \epsilon(0) (\lambda_u)^{\frac{t}{T}} \tag{5}$$

where T is the period of the QBCP. This error is doomed to grow fast: in the case of EML_2, the initial error is multiplied by a factor roughly equal to 1500 after half a period, and 2×10^6 after a full period. The EML_1 case is even worse: the error takes a factor about 21000 (resp. 5×10^8) after half a period (resp. a full period). On the contrary, in the SEM case, the unstable eigenvalues are quite small: the error is roughly

multiplied by 2 after half a period and by 4 after a full period, both in the L_1 and L_2 cases.

Such a precision shortfall is of paramount importance for the accuracy of the COC and eventually for the parameterizations of the invariant manifolds about $\mathrm{EML}_{1,2}$. In practice, the EML_1 case exhibits an overall poor precision compared to the EML_2 case.

4. THE PARAMETERIZATION METHOD IN THE QBCP

In this section, the extension of the parameterization method (PM) is introduced, with the example of the center manifold of $\mathrm{EML}_{1,2}$ as a guideline.

Note that, if not stated otherwise, the so-called *order* of the parameterization method corresponds to the order of the four-variable Taylor expansions that describe the center manifold.

4.1. Initialization of the process

In the case of $\mathrm{EML}_{1,2}$, it comes from equation (4) that

$$D\hat{F}(0) = \mathrm{diag}(\mathbf{i}\omega_1, \omega_2, \mathbf{i}\omega_3, -\mathbf{i}\omega_1, -\omega_2, -\mathbf{i}\omega_3) \tag{6}$$

Let define the three matrices H, L and N by:

$$H = \begin{pmatrix} \mathbf{i}\omega_1 & 0 & 0 & 0 & 0 & 0 \\ 0 & 0 & 0 & 0 & \omega_2 & 0 \\ 0 & \mathbf{i}\omega_3 & 0 & 0 & 0 & 0 \\ 0 & 0 & -\mathbf{i}\omega_1 & 0 & 0 & 0 \\ 0 & 0 & 0 & 0 & 0 & -\omega_2 \\ 0 & 0 & 0 & -\mathbf{i}\omega_3 & 0 & 0 \end{pmatrix}$$

with the first four columns forming L and the last two columns forming N.

In other words, L spans the 4-dimensional subspace $V^L \subset \mathbb{C}^6$ tangent to the center manifold $\mathcal{W}_c$ at the origin. The goal of the PM is here to compute a high order approximation of $\mathcal{W}_c$, starting with L as its order one approximation. Let denote $\hat{\mathbf{z}} = \hat{W}(\mathbf{s}, \theta)$ the parameterization of $\mathcal{W}_c$ where $\mathbf{s} \in \mathbb{R}^4$ are the coordinates of the manifold, and $\hat{W}(0, \theta) = 0$, $\forall\theta$.

The invariant manifold is sought in the form of a Fourier-Taylor (FT) expansion, i.e. a power series in the variable $\mathbf{s}$ whose coefficients are 2π-periodic Fourier series in the variable θ:

$$\hat{W}(\mathbf{s}, \theta) = \sum_{k \geq 1} \hat{W}_k(\mathbf{s}, \theta) \tag{7}$$

with

$$\hat{W}_k(\mathbf{s}, \theta) = \begin{pmatrix} \hat{W}_k^1(\mathbf{s}, \theta) \\ \vdots \\ \hat{W}_k^p(\mathbf{s}, \theta) \\ \vdots \\ \hat{W}_k^6(\mathbf{s}, \theta) \end{pmatrix} = \begin{pmatrix} \sum_{r \in \mathcal{R}^k} w_r^1(\theta)\mathbf{s}^r \\ \vdots \\ \sum_{r \in \mathcal{R}^k} w_r^p(\theta)\mathbf{s}^r \\ \vdots \\ \sum_{r \in \mathcal{R}^k} w_r^6(\theta)\mathbf{s}^r \end{pmatrix} \tag{8}$$

where $\mathcal{R}^k = \{r \in \mathbb{N}^4, |r| = r_1 + \cdots + r_4 = k\}$, $\mathbf{s}^r = s_1^{r_1} \ldots s_4^{r_4}$, and the coefficients $w_r^p(\theta)$ are trigonometric functions of the form:

$$w_r^p(\theta) = \sum_j w_{r,j}^p e^{\mathbf{i}j\theta} \tag{9}$$

In practice the sum (7) is truncated so that j satisfies $|j| \leq J$, with $J \in \mathbb{N}$ fixed.

The dynamics on the manifold is described by a reduced vector field $\dot{\mathbf{s}} = f(\mathbf{s}, \theta)$ for which $f(0) = 0$. The vector field f is also sought in the form of a FT series.

The couple $(\hat{W}, f)$ must satisfy the invariance equation:

$$\hat{F}\big(\hat{W}(\mathbf{s}, \theta), \theta\big) = D\hat{W}\big(\mathbf{s}, \theta\big) f\big(\mathbf{s}, \theta\big) + \frac{\partial \hat{W}}{\partial t}\big(\mathbf{s}, \theta\big) \tag{10}$$

With these ingredients, the order one $(\hat{W}_1, f_1)$ is given by:

$$\begin{cases} \hat{W}_1(\mathbf{s}, \theta) = L\mathbf{s} \\ f_1(\mathbf{s}, \theta) = \Lambda_L \mathbf{s} \end{cases} \tag{11}$$

where Λ_L is the upper left 4×4 submatrix of the diagonal matrix $\Lambda = H^{-1} D\hat{F}(0) H$.

From there, the standard procedure is to formally solve the invariance equation (10), starting from (11), by substituting the expansions of $\hat{W}$ and f in (10) and find homogeneous terms in increasing order.

4.2. The homological equations

Isolating the k-order terms in the invariance equation (10), $k > 1$, allows to get the k-order homological equation for $\hat{W}_k(\mathbf{s}, \theta)$ and $f_k(\mathbf{s}, \theta)$:

$$D\hat{F}(0)\hat{W}_k - D\hat{W}_k \Lambda_L \mathbf{s} - L f_k - \frac{\partial \hat{W}_k}{\partial t} = \left[D\hat{W}_{<k}\, f_{<k}\right]_k - \left[F\left(\hat{W}_{<k}\right)\right]_k \tag{12}$$

where the dependency in $(\mathbf{s}, \theta)$ has been omitted for the sake of clarity. The goal is to compute $\hat{W}_k$ and f_k in order to satisfy equation (12). The terms $\hat{W}_{<k}$, $f_{<k}$, and $\left[F\left(\hat{W}_{<k}\right)\right]_{<k}$ are assumed to have been obtained in previous steps.

First, the right-hand side of (12) is computed, which involves the differentiation, sum and product of Fourier-Taylor series, as well as the composition of Fourier-Taylor series with algebraic functions (in particular, the raising to a fractional power). Such operations require a complete Fourier-Taylor algebra that has been implemented from scratch in C++. For more details, see [13].

Then, following the example of [12], the normal part of (12) is separated from its tangent part. The following functions are introduced:

$$\begin{cases} \upsilon_k = H^{-1}\hat{W}_k \\ \eta_k = H^{-1}\left(\left[D\hat{W}_{<k}f_{<k}\right]_k - \left[f\left(\hat{W}_{<k}\right)\right]_k\right) \end{cases}$$

Multiplying equation (12) by H^{-1}, the homological equation then take the form:

$$\Lambda\upsilon_k - D\upsilon_k\Lambda_L\mathbf{s} - \begin{pmatrix} I_4 \\ 0 \end{pmatrix} f_k - \frac{\partial \upsilon_k}{\partial t} = \eta_k \tag{13}$$

The diagonal form of Λ allows to solve the homological equations separately on the tangent and normal spaces, spanned by υ_k^L and υ_k^N, respectively. In both cases, the adaptation to the non-autonomous case is fairly straightforward as will be detailed in [13]. In brief, the autonomous diagonal form of the linearized vector field ensures that each Fourier coefficient in the Fourier-Taylor series υ_k^p, $p \in [\![1, 6]\!]$ satisfies a simple linear differential equation in the variable θ, with the following solutions:

Normal equations. For $p = 5, 6$ and for all $r \in \mathcal{R}^k$, let $\mathbf{C}_{r,p} = \{j \in \mathbb{Z},\ j\omega_s\mathbf{i} - (\lambda_p - \lambda_L r) = 0\}$ be the set of *cross* resonances associated to (r, p), where $\lambda_L r = \lambda_1 r_1 + \cdots + \lambda_4 r_4$. It can be shown that $\mathbf{C}_{r,p} = \emptyset$, and that a solution of the homological equation is:

$$\upsilon_r^p(\theta) = \sum_{j\in\mathbb{Z}} \frac{-\eta_{r,j}^p}{j\omega_s\mathbf{i} - (\lambda_p - \lambda_L r)} e^{\mathbf{i}j\theta} \tag{14}$$

Tangent equations. For $p = 1, \ldots, 4$ and for all $r \in \mathcal{R}^k$, let $\mathbf{I}_{r,p} = \{j \in \mathbb{Z},\ j\omega_s\mathbf{i} - (\lambda_p - \lambda_L r) = 0\}$ be the set of *internal* resonances associated to (r, p). Providing that $\mathbf{I}_{r,p} = \emptyset$, a solution of this equation is:

$$\upsilon_r^p(\theta) = \sum_{j\in\mathbb{Z}} \frac{-\eta_{r,j}^p - f_{r,j}^p}{j\omega_s\mathbf{i} - (\lambda_p - \lambda_L r)} e^{\mathbf{i}j\theta} \tag{15}$$

However, the set of internal resonances is usually not empty. Fortunately, a solution can be built even in the presence of resonances by adjusting the coefficients $f_{r,j}^p$. Several strategies available in the autonomous case (denoted as *styles* [12]) are still relevant in the current context. Both styles used in this paper are detailed below: the *graph style* and the *normal form style*.

The graph style: It consists in simplifying at most the parameterization of the manifold, by taking $\upsilon_k^L = 0$ at each step. That is, for $p = 1, \ldots, 4$ and $r \in \mathcal{R}^k$: $f_r^p = -\eta_r^p$, $\upsilon_r^p = 0$.

Such a parameterization is suitable for all manifolds and is particularly adequate for center manifolds for which there exists an infinite number of internal resonances.

The normal form style: This style consists in simplifying the equations of the dynamics on the manifold, finding a normal form for f. That is, for $p = 1, \ldots, 4$, $r \in \mathcal{R}^k$, and $j \in \mathbb{Z}$:

- if $j\omega_s\mathbf{i} - (\lambda_p - \lambda_L r) \neq 0$:

$$f_{r,j}^p = 0, \quad \upsilon_{r,j}^p = \frac{-\eta_{r,j}^p}{j\omega_s\mathbf{i} - (\lambda_p - \lambda_L r)} \tag{16a}$$

- if $j\omega_s\mathbf{i} - (\lambda_p - \lambda_L r) = 0$:

$$f_{r,j}^p = -\eta_{r,j}^p, \quad \upsilon_{r,j}^p = 0 \tag{16b}$$

Implementing the normal form style implies to look not only for the zeros but also for the near-zero values of the divisors $j\omega_s\mathbf{i} - (\lambda_p - \lambda_L r)$. Indeed, numerically speaking, small values for those divisors must be avoided to ensure a certain size for the domain of practical convergence. For this reason, a threshold ε can be implemented in order to select (16a) only when the norm of the corresponding divisor is greater than ε. With such choices, the normal form style is equivalent to the Hamiltonian normal form approach developed in [6, 14], with $\varepsilon = 0.05$.

4.3. Final form

4.3.1. Graph and normal form styles

Using the graph style, the center manifold in TFC coordinates takes the form:

$$\hat{\mathbf{z}}(\mathbf{s}, \theta) = \hat{W}(\mathbf{s}, \theta) = \hat{W}_1(\mathbf{s}) + \sum_{k\geq 2}^{N} \begin{pmatrix} 0 \\ \hat{W}_k^2(\mathbf{s}, \theta) \\ 0 \\ 0 \\ \hat{W}_k^4(\mathbf{s}, \theta) \\ 0 \end{pmatrix}$$

One can see that four components of the TFC parameterization are equivalent – within a scalar factor – to the CCM coordinates, and entirely map the center manifold of dimension four. The two remaining components are given as functions of these four central components, therefore defining a graph of the form $(\hat{x}_2, \hat{y}_2) = \mathcal{G}(\hat{x}_1, \hat{x}_3, \hat{y}_1, \hat{y}_3)$. With such a form, it is straightforward to project the current state on the center manifold by using the definition (11) of $\hat{W}_1(\mathbf{s})$.

On the contrary, using the normal form style, the equivalent parameterization is a full 6×1 Fourier-Taylor vector that does not allow simple projections on the manifold.

4.3.2. *Realification of the center manifold*

Given the complexification performed in the COC, the vector $\mathbf{s}$ is complex, which does not guarantee that $W(\mathbf{s}, \theta)$ is real. It is then necessary to perform a realification, i.e. a new change of coordinates to ensure that the final result, in physical coordinates, is real. This realification is given by the following equality:

$$\tilde{\mathbf{s}} = \mathfrak{C}\,\mathbf{s} \tag{17}$$

with

$$\mathfrak{C} = \frac{1}{\sqrt{2}} \begin{pmatrix} 1 & 0 & \mathbf{i} & 0 \\ 0 & 1 & 0 & \mathbf{i} \\ \mathbf{i} & 0 & 1 & 0 \\ 0 & \mathbf{i} & 0 & 1 \end{pmatrix}$$

where $\mathbf{s} = \begin{pmatrix} s_1 & s_2 & s_3 & s_4 \end{pmatrix}^T$ are the complex reduced coordinates of the center manifold (CCM), and $\tilde{\mathbf{s}} = \begin{pmatrix} \tilde{s}_1 & \tilde{s}_2 & \tilde{s}_3 & \tilde{s}_4 \end{pmatrix}^T$ are the real ones (RCM).

Injecting (17) in the parameterization, the following real function is obtained:

$$\begin{array}{rccc} W & : & \mathbb{R}^4 \times \mathbb{R} & \rightarrow & \mathbb{R}^6 \\ & & (\tilde{\mathbf{s}}, \theta) & \mapsto & W(\tilde{\mathbf{s}}, \theta) \end{array} \quad \text{in EM coordinates}$$

Notations. For the sake of simplicity, and since there is no use of the complex parameterization (CCM coordinates) anymore, the tilde notation is skipped from now on when referring to the RCM coordinates.

4.3.3. *Comments on the energy*

In the QBCP, the huge potential well of the Sun leads to a severe drop of the order of magnitude of the energy with which the reader might be used to in the CRTBP case. As an example, the energy $H_{L_i}(t)$ of the libration orbit around $\text{EML}_{1,2}$ is always close to -847.5, in normalized EM units. To tackle this issue, the energy of any object is given with respect to the initial energy $H_{L_i}(0)$ of its associated libration periodic orbit: it is measured by the variable δH_t so that the true energy $H(t)$ satisfies $H(t) = H_{L_i}(0) + \delta H_t$. Such a relative estimate is adapted to the use of semi-analytical expansions which are inherently local.

5. DESCRIPTION OF THE NEIGHBORHOOD OF $\text{EML}_{1,2}$

5.1. Accuracy of the center manifold

The necessary tests of the precision of the parameterization of the center manifold have been focused on the estimation of the *orbital error*, defined hereafter.

Let $\mathbf{z}(t)$ and $\mathbf{s}(t)$ be the solutions of the Cauchy problem $\dot{\mathbf{z}} = F(\mathbf{z})$, $\mathbf{z}(0) = \mathbf{z}_0 = W(\mathbf{s}_0, 0)$ and $\dot{\mathbf{s}} = f(\mathbf{s})$, $\mathbf{s}(0) = \mathbf{s}_0$, respectively. Then, the orbital error e_O at time t is defined as:

$$e_O(t, \mathbf{s}_0) = |W(\mathbf{s}(t)) - \mathbf{z}(t)|_\infty$$

The orbital error has to be measured on small time spans, since the hyperbolic directions produce exponential errors (see subsection 3.3). In the present paper, the orbital error has been computed up to $t = 1$, as in [14]. Let $e_O^1 := e_O(t = 1)$, for the sake of brevity. For such a time span, any numerical error on the initial conditions is amplified by a factor of 10 (resp. 20) in the EML_2 (resp. EML_1) case.

Since we are working in manifolds of order four or higher, the systematic testing of any kind of error in the complete phase space is a tremendous computational task. Thus, as a first step, one may arbitrarily decrease the number of dimensions along which the error is evaluated. Such "cuts" in the phase space are common for these types of tests (see e.g. [14]). After an extensive test campaign involving various cuts, it has been found that the following set of initial conditions acts as a bordeline case for the accuracy of the center manifold, both in the L_1 and L_2 cases:

$$\mathcal{S}_{-1} = \{(\mathbf{s}_0, t_0 = 0) \text{ with } \mathbf{s}_0 = (s_1\ 0\ -s_1\ 0)^T,\ s_1 \in \mathbb{R}\}$$

Given that $s_2 = s_4 = 0$, the motion is restricted to the xy-plane in EM coordinates. Moreover, the condition $s_1 = -s_3$ imposes the initial state $\mathbf{z}_0 = W(\mathbf{s}_0, 0)$ to be on the x-axis.

5.1.1. EML_2 *case*

Figure 3 gives the orbital error e_O^1 for the set $\mathcal{S}_{-1}$ of initial conditions, as a function of the x coordinate. The position of EML_2 is given by the point of minimum error, around $x = -1.165$. The following comments can be made:

- Within the domain of practical convergence, the precision appears to tend to a limit as the order increases. In particular, there is not much improvement for orders higher than 20 or 22, which is the reason why higher orders have not been displayed.

- More importantly, the radius of practical convergence is undoubtedly better in the graph case. Looking at Figure 3a, one can clearly see the limits of the domain of practical convergence at $x_1 = -1.175$ and $x_2 = -1.13$. Those values correspond exactly to the four $T/2$-periodic resonant orbits highlighted in [14], and denoted PO2a-d (see Figure 2b therein). As usual, such low order resonances tend to introduce small divisors in the semi-analytical algorithms and therefore act as a natural obstruction to the existence of a good parameterization. However, the use of the graph style allows to limit to the bare minimum the number of small divisors involved in the solving of the homological equations (see 4.2). Consequently, the domain of practical convergence is increased, as can be seen on Figure 3b.

These remarks remain true for all tested sets of initial conditions.

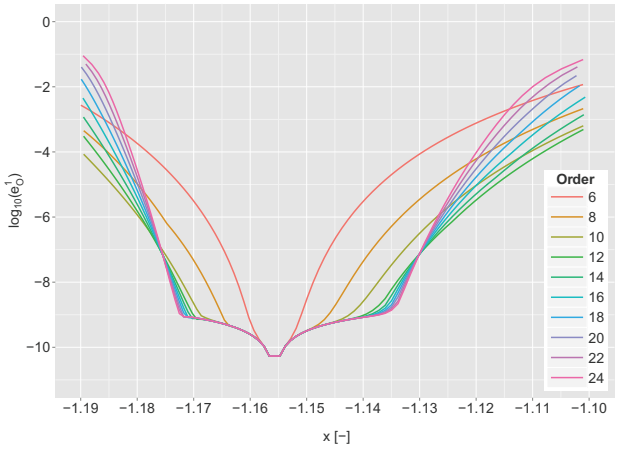

(a) Normal form style

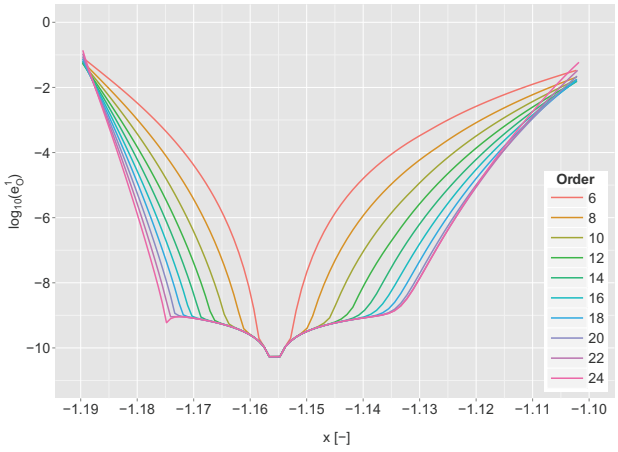

(b) Graph style

Fig. 3: The orbital error e_O^1 for the set $\mathcal{S}_{-1}$ of initial conditions, as a function of the x coordinate, for various orders of the parameterization of the center manifold of EML_2.

5.1.2. EML_1 *case*

In the EML_1, the differences between both styles tend to vanish, mainly because there is no known resonant orbit in the close vicinity of the libration point that would have played a role similar to PO2a-d. Moreover, the overall precision is worse than in the EML_2 case because the EML_1, as anticipated in subsection 3.3. In particular, numerical simulations in the worst case show that there is not much improvement for orders higher than 16. On the bright side, there is room for improvement since the source of the imprecision has already been identified as the COC instability, which may be partially handled numerically.

5.2. Projection method

All the subsequent solutions within the center manifold have been computed using the projection method, described in details in [12]. In brief: for any initial conditions $\mathbf{s}_0$ in the center manifold, the initial conditions $\mathbf{z}_0$ in EM coordinates are obtained at time t_0 applying $\mathbf{z}_0 = W(\mathbf{s}_0, \omega_s t_0)$. Then, the state is integrated using the 6-dimensional physical vector field, until time $t = t_1$. Due to numerical instabilities produced by the hyperbolic directions, the overall error tends to grow. Hence, the current state $\mathbf{z}(t_1)$ can be projected on the parameterized center manifold, which provides a new vector $\mathbf{s}_p$. The state $\mathbf{z}_p = W(\mathbf{s}_p, \omega_s t_1)$ is then used to start the next integration phase.

In the context of integration by projection, one can get a rough idea of the precision of each solutions by computing the magnitude $e_P(t_1)$ of the correction performed at each projection, defined as:

$$e_P(t_1) = |\mathbf{z}(t_1) - \mathbf{z}_p(t_1)|_\infty \tag{18}$$

Note that the change of variables involved in the projection process is particularly easy to perform using the graph style, as it has been shown in paragraph 4.3.1.

5.3. Variations of the energy

Contrary to the CRTBP case, the energy is not constant along a solution inside the center manifold. In order to get an estimation of the variations of the energy, the xy-planar stroboscopic maps of the center manifold of $\text{EML}_{1,2}$ have been computed. Namely, for each initial condition of the form $\mathbf{s}_0 = \begin{pmatrix} s_1 & 0 & s_3 & 0 \end{pmatrix}^T$, $t_0 = 0$, the EM equations of motion are numerically integrated and a point is stored each time the trajectory crosses the section $t = 0\ [T]$, with T the period of the QBCP. Selecting only the points for which $t = 0\ [T]$ erase all variations ought to the T-periodic behavior of the coefficients that appear in the Hamiltonian (1).

For each individual orbit, the mean energy $\mu(\delta H)$ has been computed along with the associated standard deviation $\sigma(\delta H)$. The corresponding results are presented on Figure 4. On this figure, the greater the mean energy, the bigger the orbit. For instance, a mean energy around 0.005 corresponds to a mean distance from the libration point of about 17000 km (resp. 13000 km) in the EML_2 (resp. EML_1) case. The stroboscopic maps have been computed in the mean mean energy range $[0, 0.011]$, which encloses the Halo orbit bifurcation for both libration points (see section 5.4).

EML_1 case. The standard deviation is a smooth increasing function of the mean energy value. Moreover, $\sigma(\delta H)$ is never greater than 10% of the mean energy, except for very small values of the energy. As an example, $\sigma(0.01)$ is about 3% of $\mu(0.01)$.

EML$_2$ **case.** For values of the energy smaller than 0.006, and as the mean energy increases, the standard deviation is more or less converging to 10% of the mean energy.

Around $\mu(\delta H) \simeq 0.006$, the standard deviation breaks down, which corresponds to the solutions that cross the $2\omega_s$ resonance. After this resonance, starting from $\sigma(\delta H) = 0$, the standard deviation regains its smoothness with respect to the mean energy.

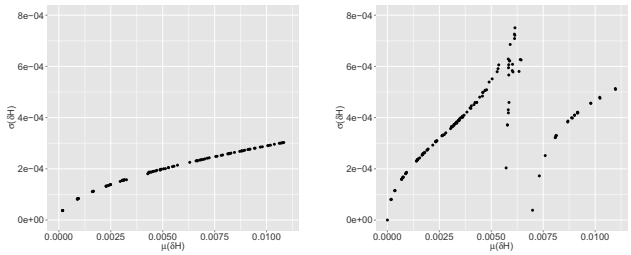

(a) EML$_1$ case (b) EML$_2$ case

Fig. 4: Standard deviation σ of the energy $\delta H(t)$ as a function of the mean value μ of the energy for some solutions of the planar stroboscopic maps.

5.4. Poincaré maps

Poincaré maps provide a qualitative insight into the dynamics inside a center manifold. In this paper, Poincaré maps with a Poincaré section of the form $z = 0$, $p_z > 0$ have been computed in the EML$_{1,2}$ case. Such sections are also usually used in the CRTBP autonomous case [8, 12]. In the latter context, an additional condition on the energy of the form $\delta H_0 = h$ allows to produce two-dimensional Poincaré maps.

In the QBCP case, the energy is no longer constant but its variations remains bounded for any solution in the center manifold, in proportions similar to the results of Figure 4. Hence a relaxed version of the energy condition may be defined: $|\delta H_0 - h| \leq \sigma^c(h)$, with $\sigma^c(h)$, a given "energy thickness", representative of the energy variations associated with an initial energy around h. The underlying idea is to define an energy layer such that all solutions that have an initial energy within this layer maintain their energy in it.

In this paper, the "super" constraint $\sigma^c(h) = 0$ has been imposed in order to limit the number of solutions displayed on the maps. Consequently, looking at a given map, one has to recall that (i) the energy is not constant but bounded along the trajectories (with a maximum deviation around 10%), and (ii) the range of displayed solutions is a representative but non-exhaustive set of solutions inside this energy layer.

In practice, the following process is used to compute the maps: the initial time is set equal to zero. Then, an initial energy value h and a point (s_1, s_3) are selected. Moreover, the condition $s_2 = s_4$ is imposed, which, with the graph style and the current choice of COC, guarantees that $z(t = 0) = 0$ in EM coordinates. Imposing $\delta H_0 = h$, the corresponding $s_2 = s_4$ value is computed. Then, this point is used as initial condition for a numerical integration of the equations of motion, plotting a point each time that the trajectory crosses the plane $z = 0$, $p_z > 0$. For each of these points, the projection method is used to reinitialize the state on the center manifold, and the projection error $e_P(t)$ is estimated. The precision $e_P(t) = 10^{-6}$ is taken as an arbitrary reference accuracy. In practice, it corresponds to a maximum error of about 50 meters in position and 10^{-4} meters per second in velocity.

5.4.1. EML$_2$ *case*

The results can be seen on Figure 5, for small values of the energy. All solutions comply with the condition $e_P(t) < 10^{-6}$. Contrary to the autonomous case, some solutions overlap. In particular, the overlapping seems to increase with the initial energy, which is consistent with the fact that the standard deviation of the energy tends to grow with its mean value.

On each plot, several solutions exhibits specific variation patterns (see for example the innermost green solution of Figure 5c). These patterns are present also when the integration of the equations of motion is performed directly with the reduced vector field. Therefore the discontinuities introduced by the projection method cannot be held responsible for such variations, which are truly characteristic of the periodically-perturbed system.

In order to test the limit of the description provided by the parameterization method, equivalent Poincaré maps have been computed for higher initial energies. The corresponding results are given on Figure 6. For these two plots, the condition $e_P(t) < 10^{-6}$ have been relaxed (see caption), but the points that indeed comply with this constraint are displayed in green. As one would expect, it is clear that the precision worsens as the energy increase. Such precision shortage is expected, in particular in the EML$_2$ neighborhood which corresponds to higher energies than the EML$_1$ case, in absolute. In particular, it seems difficult to achieve a very good accuracy during the computation of quasi-halo orbits. Even if their influence is reduced by the graph style implementation, it is probable that the orbits resonant with the Sun still participate in the numerical error. A remaining challenge is to dissociate the contribution of the latter to the error from the natural precision decay inherent to the three-body EML$_2$ case.

5.4.2. EML$_1$ *case*

The results for the EML$_1$ case are given on Figure 7. The same remarks apply. In particular, high energies require the condition $e_P(t) < 10^{-6}$ to be slightly relaxed. However, the halo orbit bifurcation is more easily obtained. Such a difference may be ought to two factors. First, the Halo bifurcation happens for an energy smaller than in the EML$_2$ case, both with

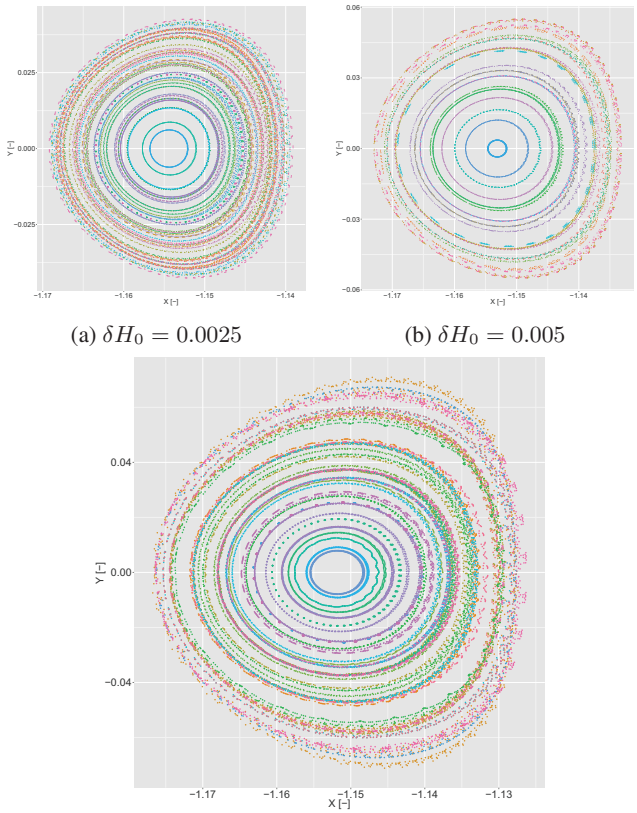

(a) $\delta H_0 = 0.0025$ (b) $\delta H_0 = 0.005$

(c) $\delta H_0 = 0.0075$

Fig. 5: Low-energy Poincaré maps in the EML_2 case, in EM coordinates. All solutions comply with the condition $e_P(t) < 10^{-6}$. The color scale is just here to visually distinguish the solutions.

respect to the libration point and in absolute. Then, there is no known resonances with the Sun in the close vicinity of the

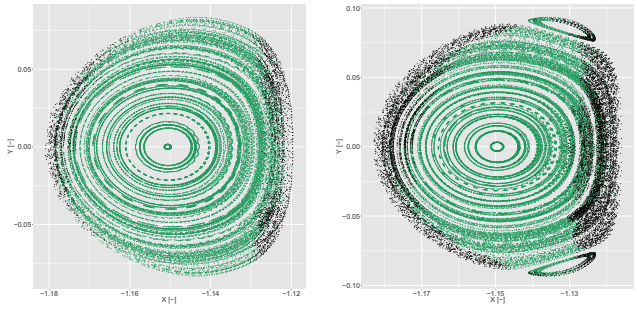

(a) $\delta H_0 = 0.01$ (b) $\delta H_0 = 0.012$

Fig. 6: High-energy Poincaré maps in the EML_2 case. In green: all points that satisfy $e_P(t) < 10^{-6}$. (a) All displayed solutions comply with $e_P(t) < 10^{-4}$. (b) All solutions satisfy $e_P(t) < 10^{-3}$.

EML_1 which could act as a natural obstruction to the semi-analytical description of this neighborhood. Additional simulations show that, at higher energy, a precision decay very similar to the one displayed on Figure 6 occurs in the EML_1 case, which tends to back up the first hypothesis.

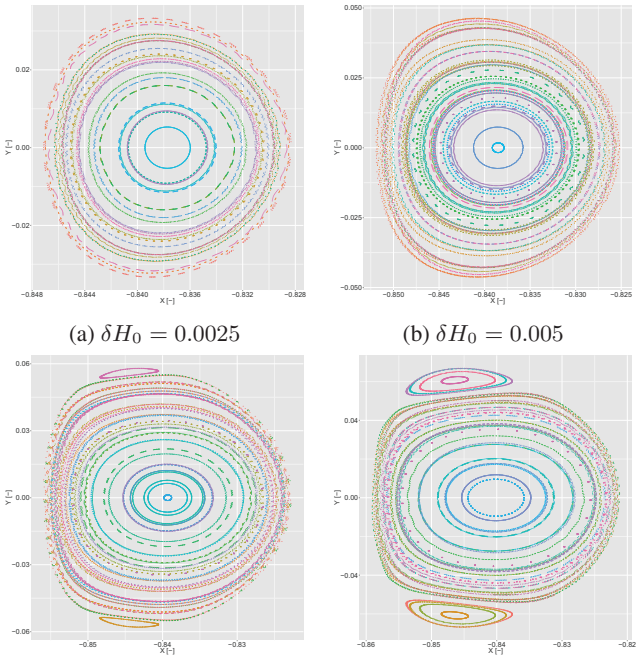

(a) $\delta H_0 = 0.0025$ (b) $\delta H_0 = 0.005$

(c) $\delta H_0 = 0.0075$ (d) $\delta H_0 = 0.01$

Fig. 7: Low-energy Poincaré maps in the EML_1 case, in EM coordinates. On (a), (b): all solutions comply with the condition $e_P(t) < 10^{-6}$. On (c), (d): all solutions comply with the condition $e_P(t) < 10^{-5}$. The color scale is just here to visually distinguish the solutions.

6. CONCLUSION

In this paper, the parameterization method (PM) has been applied to obtain high-order semi-analytical approximations of invariant manifolds about the dynamical equivalents of the collinear libration points in the Sun-perturbed Earth-Moon system, viewed as a Quasi-Bicircular Problem. The overall process can be seen as an extension of previous works in the CRTBP [12, 15]. Both the method and its applications have been focused on the comparison with normal form computations in the Sun-Earth-Moon QBCP, more specifically in the EML_2 case [6, 14]. It has been shown that the advantages of the parameterization methods are particularly relevant in this context. More specifically:

- The different *styles* available in the PM bring more flexibility to the user, compared to the normal form computations over the Hamiltonian. In particular, the graph

style allows to keep to a minimum the number of potential small divisors during the computation of the semi-analytical approximations. The visible consequence is that some specific resonances with the Sun are better handled, although they most likely still act as a obstruction for the domain of practical convergence.

- The graph form of the parameterization provides a very simple change of coordinates between the physical variables and the reduced coordinates. This allows to easily project the current state on the center manifold which in turns speeds up the numerical integrations.

- Finally, from a pure numerical perspective, the parameterization method allows to manipulate 4-dimensional Taylor series. On the contrary, the normal form procedure is performed on the 6-dimensional complete state. Working with the parameterization method allows to reduce the dimension of the Fourier-Taylor series, which can be critical at high order, when millions of scalar coefficients are involved.

In spite of these advantages, results on Poincaré maps show that the EML_2 quasi-Halo orbits are still difficult to obtain semi-analytically. On the contrary, they have been more easily computed in the EML_1 case, despite the limited accuracy of the associated change of coordinates (2) that limits the highest available order for the parameterization.

Indeed, the precision of the T-periodic functions that are used throughout the procedure act as a bottleneck for the overall accuracy of the parameterization. Improving these functions would benefit the whole process and help understand how well the resonances are actually handled by this new implementation.

7. REFERENCES

[1] C. Simó, G. Gómez, À. Jorba, and J. Masdemont, "The bicircular model near the triangular libration points of the RTBP," *From Newton to Chaos*, pp. 343–370, 1995.

[2] G. Gómez, À. Jorba, J. Masdemont, and C. Simó, *Dynamics and Mission Design near Libration Points IV*, 2001.

[3] G. Mingotti, F. Topputo, and F. Bernelli-Zazzera, "Efficient invariant-manifold, low-thrust planar trajectories to the Moon," *Communications in Nonlinear Science and Numerical Simulation*, vol. 17, no. 2, pp. 817–831, 2012.

[4] Kazuyuki Yagasaki, "Sun-perturbed earth-to-moon transfers with low energy and moderate flight time," *Celestial Mechanics and Dynamical Astronomy*, vol. 90, no. 3-4, pp. 197–212, 2004.

[5] F. Topputo, "On optimal two-impulse Earth-Moon transfers in a four-body model," *Celestial Mechanics and Dynamical Astronomy*, vol. 117, no. 3, pp. 279–313, 2013.

[6] M. A. Andreu, *The quasi-bicircular problem*, Ph.D. thesis, 1998.

[7] G. Gómez and J. M. Mondelo, "The dynamics around the collinear equilibrium points of the RTBP," *Physica D: Nonlinear Phenomena*, vol. 157, no. 4, pp. 283–321, 2001.

[8] À. Jorba and J. Masdemont, "Dynamics in the center manifold of the collinear points of the restricted three body problem," *Physica D: Nonlinear Phenomena*, vol. 132, no. 1, pp. 189–213, 1999.

[9] E. Castella Carlos and À. Jorba, "On the vertical families of two-dimensional tori near the triangular points of the bicircular problem," *Celestial Mechanics*, vol. 76, no. 1, pp. 35–54, 1999.

[10] F. Gabern, "Effective Computation of the Dynamics Around a Two-Dimensional Torus of a Hamiltonian System ‘," pp. 1–24, 2005.

[11] A. Farrés and À. Jorba, "On the High Order Approximation of the Centre Manifold for Odes," *Discrete And Continuous Dynamical Systems Series B*, vol. 14, no. 3, pp. 977–1000, 2010.

[12] A. Haro, *The parameterization method for invariant manifolds: from rigorous results to effective computations*, To appear, 2016.

[13] B. Le Bihan, J. Masdemont, G. Gómez, and S. Lizy-Destrez, "The parameterization method for invariant manifolds in the Quasi-Bicircular Problem," *In preparation*.

[14] M. A. Andreu, "Dynamics in the center manifold around L2 in the quasi-bicircular problem," *Celestial Mechanics and Dynamical Astronomy*, vol. 84, pp. 105–133, 2002.

[15] X. Cabré, E. Fontich, and R. De La Llave, "The parameterization method for invariant manifolds III: overview and applications," *Journal of Differential Equations*, vol. 218, no. 2, pp. 444–515, 2005.